Appl. Phys. B 75, 3–13 (2002)
DOI: 10.1007/s00340-002-0957-x

Applied Physics B
Lasers and Optics

Invited paper

H. HILLMER[1,✉]
J. DALEIDEN[1]
C. PROTT[1]
F. RÖMER[1]
S. IRMER[1]
V. RANGELOV[1]
A. TARRAF[1]
S. SCHÜLER[1]
M. STRASSNER[2]

Potential for micromachined actuation of ultra-wide continuously tunable optoelectronic devices

[1] Institute of Microstructure Technologies and Analytics (IMA) and Centre for Interdisciplinary Nanostructure Science and Technology (CINSaT), University of Kassel, Germany
[2] KTH, Royal Institute of Technology, Kista, Sweden

Received: 10 May 2002
Published online: 8 August 2002 • **© Springer-Verlag 2002**

ABSTRACT Tailored scaling represents a principle of success that, both in nature and in technology, allows the effectiveness of physical effects to be enhanced. Mutation and selection in nature are imitated in technology, e.g. by model calculation and design. Proper scaling of dimensions in natural photonic crystals and our fabricated artificial 1D photonic crystals (DBRs, distributed Bragg reflectors) enable efficient diffractive interaction in a specific spectral range. For our optical microsystems we illustrate that tailored miniaturization may also increase the mechanical stability and the effectiveness of spectral tuning by thermal and electrostatic actuation, since the relative significance of the fundamental physical forces involved considerably changes with scaling. These basic physical principles are rigorously applied in micromachined 1.55-μm vertical-resonator-based devices. We modeled, implemented and characterized 1.55-μm micromachined optical filters and vertical-cavity surface-emitting laser devices capable of wide, monotonic and kink-free tuning by a single control parameter. Tuning is achieved by mechanical actuation of one or several air-gaps that are part of the vertical resonator including two ultra-highly reflective DBR mirrors of strong refractive index contrast: (i) $\Delta n = 2.17$ for InP/air-gap DBRs (3.5 periods) using GaInAs sacrificial layers and (ii) $\Delta n = 0.5$ for Si_3N_4/SiO_2 DBRs (12 periods) with a polymer sacrificial layer to implement the air-cavity. In semiconductor multiple air-gap filters, a continuous tuning of $> 8\%$ of the absolute wavelength is obtained. Varying the reverse voltage ($U = 0$–5 V) between the membranes (electrostatic actuation), a tuning range of > 110 nm was obtained for a large number of devices. The correlation of the wavelength and the applied voltage is accurately reproducible without any hysteresis. In two filters, tuning of 127 and 130 nm was observed for about $\Delta U = 7$ V. The extremely wide tuning range and the very small voltage required are record values to the best of our knowledge. For thermally actuated dielectric filters based on polymer sacrificial layers, $\Delta\lambda/\Delta U = -7$ nm/V is found.

PACS 85.60.Jb; 85.30.De; 85.30.Kk, 42.79.Ci; 77.55.+f; 78.66.Fd

1 Introduction

Approaching optimum functionality in the design of optical, mechanical and electronic components always requires characteristic structure sizes to be tailored according to key quantities of fundamental physics. For obtaining a distinct diffraction by an optical grating, it is necessary, for example, for the grating period to be in the same order of magnitude as the light wavelength [1]. To achieve a proper operation of field-effect transistors, for example, the length of the gate electrode has to be in the same order of magnitude as the carrier diffusion length. Thus, the structure size has to be carefully designed in consideration of carrier lifetime, carrier mobility and carrier densities. Concerning the field effect transistor operation, the importance of miniaturization in semiconductors [2] or the increase in temperature and the decrease in structure size of alkali halides [3] has been recognized very early. Further examples are mentioned below. This paper intends to demonstrate this principle also for special microsystems in which microoptics, micromechanics and microelectronics are combined and which may hold a very large potential for future optical communications.

Advanced long-haul optical 1.55-μm or 1.3-μm communications systems require diverse high-quality active and passive optoelectronic components, preferentially tailored to achieve high functionality and specific device properties. The ultra-high bit-rate capacity required can be obtained, for instance, by dense wavelength division multiplexing (DWDM), i.e. by using a large number of spectrally closely neighbored and independently modulated transmission channels. Recently, vertical microresonator based devices such as filters and vertical-cavity surface-emitting lasers (VCSELs) have become very attractive for DWDM systems. In this field, widely and continuously tunable 1.55-μm optoelectronic devices based on a single control parameter are highly desirable, but very difficult to implement. Another difficulty is the implementation of the required ultra-highly reflective Bragg mirrors (distributed Bragg reflectors, DBRs) in that wavelength range.

As far as filters are concerned, many different approaches and material systems have been implemented. Among the multiple-layer-based devices, bulk-like and non-tunable components are absolutely dominant. Only a few devices are macromechanically tunable. Very rare are surface-micromachined tunable components: AlAs/AlGaAs [4, 5], GaInAs/InP [6] and Si-SiO_2-TiO_2 [7] and bulk-micromachined two-chip devices: AlAs/GaAs [8].

In the literature, many promising and interesting concepts concerning VCSELs can be found. Absolutely dominating

✉ Fax: +49-561/804-4488, E-mail: hillmer@uni-kassel.de

are lasers with emission wavelengths below 1 μm. Although 1.55-μm VCSELs are highly desirable, only very few implementations have been reported up to now: GaInAsP VCSELs with fused AlAs/GaAs DBRs [9, 10], GaInAsP VCSELs with metamorphic AlAs/GaAs DBRs [11], highly efficient AlGaInAs VCSELs [12] and AlGaInAs VCSELs with AlAsSb/AlGaAsSb DBRs [13]. These electrically pumped devices are not tunable at the moment, apart from the option of temperature variations. In addition, a non-tunable optically pumped 1.26-μm multiple air-gap GaInAsP VCSEL has been reported [14]. Micromachined GaAs VCSELs have shown a tunability of 18 nm [15] and 31.6 nm [16]. For 1.55-μm devices, concepts [8, 16–21] based on micromachining technologies and enabling tunability via micromachined actuation have been applied very rarely, although the principles were successfully demonstrated in the GaAs material system as early as 1995 [4, 5, 13].

This paper deals with micromachined 1.55-μm vertical-resonator-based devices enabling both a wide tunability based on a single control parameter and highly reflective DBRs. To achieve this with a minimum number of Bragg periods, we combine materials having a very strong refractive index contrast. We focus on two material systems: InP/air-gap DBRs and Si_3N_4/SiO_2 DBRs. Membrane/air-gap structures are attractive due to their inherent large refractive index contrast. However, these membrane-based systems raise questions of mechanical stability.

Therefore, fundamental physical properties are studied qualitatively in Sect. 2 as a function of structure size. The results of these qualitative studies underline the need for miniaturization if we intend to increase the mechanical stability and spectral tunability of the optoelectronic components obtained by micromachined actuation. We study physical aspects of the efficiency of electrostatic and thermal actuation and their potential in cases where the harmful influence of inertia and gravity forces is tremendously reduced to avoid material fatigue. In Sect. 3, the optical properties of Bragg mirrors are investigated in order to optimize the maximum spectral mirror reflectance as a function of the number of periods, considering different values of material absorption. Different material systems are compared for the purpose of achieving a high reflectance with a minimum total layer thickness. The principles of electrostatic tuning are discussed in Sect. 4, while Sect. 5 deals with device fabrication using surface micromachining and sacrificial layer techniques. These methods allow devices including actuable parts to be batch-processed without any need for expensive mechanical micromounting at the end of the fabrication process. Sections 6 and 7 present experimental and theoretical results such as reflectance spectra, tuning efficiencies and tuning ranges. Finally, the results are summarized.

2 Tailored scaling, a principle of success in nature

Physics strongly correlates structure sizes and phenomena associated with interactions. First, the crucial importance of structure size will be illustrated by light interacting with structured solids. In the following, we will briefly mention three different possibilities of physical interactions. Let us consider monochromatic light of, say, 3-μm wavelength interacting with an optical grating. In a first scenario, we assume an amplitude grating having a period considerably larger (e.g. 3 cm) than the wavelength. The resulting distinct shadows projected by the opaque lines on a screen are well known in our daily life, for instance, from bridge railings illuminated by sunlight. In a second scenario in which the grating period is in the same order of magnitude as the wavelength, we observe diffraction patterns, i.e. the Fourier transformation of the grating, on a screen. The last scenario involves a phase grating consisting of transparent ridges alternating with transparent grooves, the grating period of which is, for instance, 30 nm. In this case, the grating acts as an artificial quasi-layer, which exactly coincides in thickness with the grating height (thickness). Since the refractive index of this layer is determined by the duty cycle of the grating and the refractive indices involved, artificial materials with tailored refractive indices can be implemented by the definition of structure sizes. Hence, the effectiveness of physical effects is determined by tailored scaling of structure sizes.

Photonic or acoustic crystals are further examples of the interaction of electromagnetic waves (e.g. light) or acoustic waves with periodic structures. Natural opals show wonderful opalescent colors, which change whenever these natural 3D photonic crystals are rotated. The wings of very rare exotic butterfly species include 1D photonic crystal structures composed of periodic multiple layers of alternating refractive indices. These insects are able to change the color of their wings by tilting the wings with respect to the positions of the sun and the eye acting as a detector. In this case again, the periodicity of the structures is in the same order of magnitude as the light wavelength. In physics, these phenomena are explained by constructive interference occurring in the case of specific angles and wavelengths according to the Bragg condition.

A very recent investigation started by our group concerns the quetzal (the resplendent bird depicted in the flag of the state of Guatemala), which mainly lives in the rain forests of Central America. Vertical incidence of light on the wings and an observation angle of zero degrees yield a yellow-color impression. Increasing the observation angle from 0° to 90° changes the color impression continuously from yellow to green to blue and finally to violet. Photonic crystals also seem to be involved in this case. Further investigations are under way in our group.

In summary, optical, mechanical and electronic components can be optimized if characteristic structure sizes are designed and tailored according to key quantities of fundamental physics. Physics behind recipes for success in nature are inspiring models for scientists and engineers using advanced and interdisciplinary methods. Mutation and selection in nature are imitated and copied by model calculation and design in technology. Thus, bionics can be a very interesting field offering an enormous potential for the future. The filter and VCSEL structures implemented and studied in this paper are very closely related to the exotic butterfly and quetzal wings, since they do not represent 1D natural, but 1D artificial, photonic crystals. Before going into the technology and characterization of these devices, we will give a few general considerations related to the size of those structures, i.e. microsystems.

These membrane/air-gap structures (see Figs. 3–6 below) are attractive due to their inherent large refractive index contrast. At a first glance, however, the mechanical stability does not seem to be very high. In our macro world, strong accelerations and decelerations cause noticeable fatigue of material due to the harmful influence of inertia and gravity forces. All physical quantities depend in different ways on space coordinates. Thus, the relative significance of fundamental physical forces considerably varies with structure size. This is studied by scaling each direction in space x_i ($i = 1, 2, 3$) by the same factor $1/a$ by replacing $x_i \rightarrow x_i/a$. Miniaturization increases with growing a (magnification would increase with decreasing a). Disregarding effects mentioned below, we find the following potential relations: gravity force $\sim a^{-3}$, inertia force $\sim a^{-4}$, magnetic force $\sim a^{-2,\dots,4}$, electrostatic force $\sim a^{-0,\dots,2}$ and thermal expansion force $\sim a^{-2}$. Figure 1 schematically depicts these forces as a function of the scaling factor in a double-logarithmic plot. If, in addition, material constants become dependent on dimensions and quantization effects in electron, phonon and photon systems are involved, there will be no strict potential law ($\sim a^{-n}$) for the electrostatic, the magnetic and the thermal expansion forces. Examples of systems of the above-mentioned variable dimensionality (3D, 2D, 1D, 0D) are photonic crystals, quantum wells (QWs), quantum wires, quantum dots and systems containing slab phonons. The absence of such potential laws ($\sim a^{-n}$) will cause the straight lines in the diagram to be bent, i.e. the exponent n may vary with the structure size. In the case of the electrostatic force, the exponent may vary between 0 and 2, depending on the specific situation. For the magnetic force, the variation of the exponent may range from 2 to 4. For a demonstration of the principle as intended in this paper, however, these details are of minor importance. For the schematic plot shown in Fig. 1, the potential relations $a^{-1.5}$ and a^{-4} have been chosen as an example for the electrostatic and magnetic forces, respectively. In addition, the absolute values of the forces depend on the geometries and materials of all components of the system considered. Thus, varying the ratio between length, width and height of a mechanical membrane, for instance, will slightly shift the lines in the vertical direction relative to each other. Similar shifts would occur if materials are exchanged.

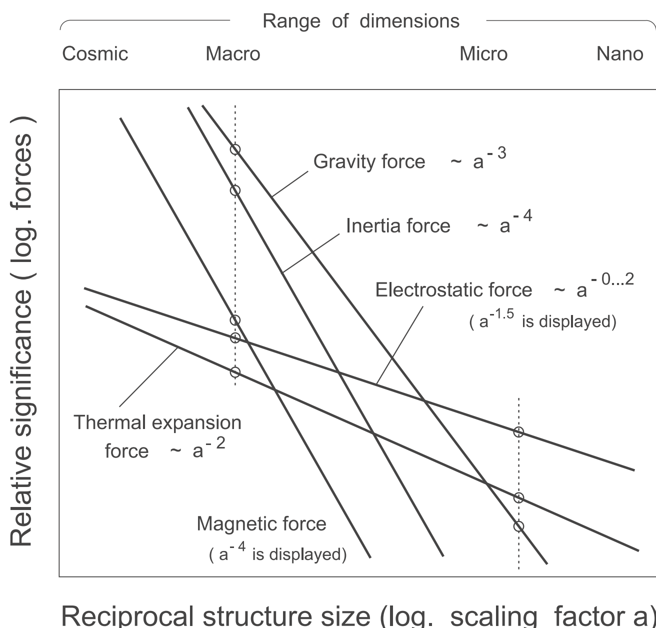

FIGURE 1 Schematic diagram visualizing scaling of fundamental forces

In the following, we will qualitatively compare the relative significance of the above-mentioned forces for a hypothetical system in which forces are assumed to scale with structure size according to Fig. 1. Next, two systems are assumed which are identical in proportions and materials, but differ considerably in size. The *macro*system is indicated in Fig. 1 by the vertical dotted line on the left; the *micro*system by the dotted line on the right. For the *micro*system, electrostatic and thermal expansion forces dominate. In the *macro*system these forces play a less important role and gravity as well as inertia forces dominate. The latter cause fatigue of the material in the presence of strong accelerations and a weakly supported long cantilever structure, for instance.

In our *macro* world electrostatic and magnetic forces are of comparable magnitude, enabling constructions such as our well-known electro-motors. However, these motors do not work if they are excessively miniaturized or magnified. Among electro-motors of identical structure which are 10 km, 10 cm or 10 nm in size, only those we are familiar with (e.g. 10 cm in size) will work. The ultra-large motor (10 km in size) would suffer from a too weak electrostatic force. The ultra-small version (10 nm in size) would not rotate since the magnetic forces are too small. To implement ultra-small motors the electrostatic comb actuator principle is applied [22], which does not involve magnetic forces.

Note that in cosmic systems mass attraction becomes very dominant. With strongly increasing size the potential relation of the gravity force will continuously change from a^{-3} to a^{-4}. The latter case represents astrophysical situations (planets, moons, solar systems). However, the range shown in Fig. 1 refers to a system much smaller than the planets and it implies an unchanged gravity constant. This means that the planet itself is not scaled. In the case of scaling both, the system and the planet, a relation a^{-6} will result.

Most interesting is the fact that the electrostatic force depends much less on scaling (or is even insensitive to scaling if the exponent 0 comes into play) than the inertia and gravity forces. Note that a small dust particle electrostatically sticking to the ceiling overcompensates for the gravity force. In micro- and nanosystems, gravity and inertia forces become very small relative to other forces. This means that increasing miniaturization makes systems more and more stable. Note that it is very easy to break an (empty!) wine glass by dropping it to the floor. It is still easy to break a larger one of the fragments. However, it becomes increasingly difficult to break and divide the very small fractions of this glass a second and a third time by dropping them to the ground. Hence, inertia forces, which are mainly responsible for breaking, become significantly weaker with miniaturization. Thus, tailored miniaturization supports a tremendous stability increase of micro- and nanosystems and enables dominating roles of electrostatic and thermal forces. Therefore, these forces seem to be very attractive for actuation in micro- and nanosystems. The essential message of

this section is: an appropriate choice of the system size allows the relative significance of the physical phenomena involved to be changed and specific desired system features to be tailored.

Our microsystems reported below take advantage of the fact that miniaturization increases the effectiveness of electrostatic and thermal expansion forces while, at the same time, the harmful influence of inertia and gravity forces is reduced. This contributes to preventing fatigue of the material making up the structures.

3 Highly reflective Bragg mirrors

A single DBR mirror (left inset in Fig. 2) consists of an alternating sequence of two different material layers. Two neighboring layers define a period of optical thickness $m_P\lambda/2$ ($m_P = 1, 2, ...$). In our paper, each individual DBR layer has a thickness of $m_i\lambda_i/4$ ($m_i = 1, 3, ...$) where λ_i is the material wavelength of material i (λ in air is 1.55 µm). Using transfer-matrix calculations, the reflectance has been calculated as a function of wavelength for different p and different material absorption coefficients α. The spectral variation $\alpha = \alpha(\lambda)$ is taken into account. The right inset in Fig. 2 shows the spectral reflectance for a Si_3N_4/SiO_2 DBR ($p = 12$, $\lambda_i/4$ layers, $\alpha = 0$). The maximum spectral reflectivity R_{max} at $\lambda = 1.55$ µm (see arrow) is evaluated from the individual spectra calculated for Si_3N_4/SiO_2 and InP/air-gap DBRs and plotted in Fig. 2 as a function of the number of periods p. Series of spectra are calculated for Si_3N_4/SiO_2 DBRs with varying absorption loss $\alpha = 0, 0.1, 0.3, 1, 3, 10, 20, 100\,cm^{-1}$. Note that α markedly depends on the technological fabrication and the process parameters in these amorphous materials. In contrast, optical loss in semiconductor material dominantly depends on the band structure in high-quality crystalline material. Therefore, material loss is far better known quantitatively in the latter material class. Figure 2 shows that the maximum spectral reflectance R_{max} of a DBR strongly increases with p, but saturates for higher values. The saturation level of R_{max} strongly decreases with increasing loss. The stop-band represents the extended spectral region of high reflectivity (i.e the spectral plateau-like structure in the inset of Fig. 2).

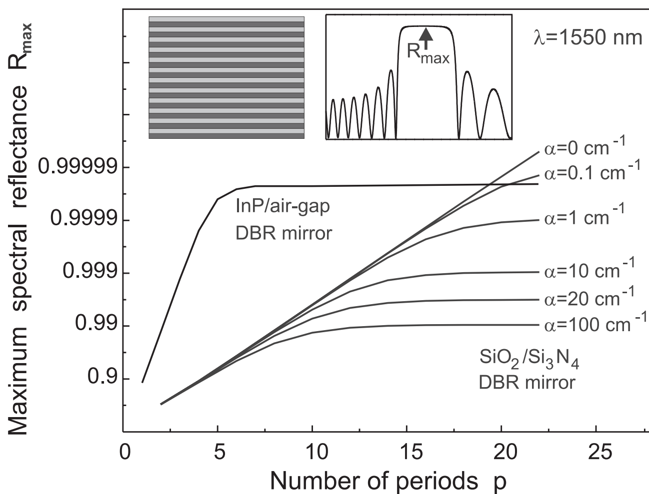

FIGURE 2 Calculated maximum spectral reflectance versus periods p with loss as a variation parameter; *left inset*: DBR mirror structure, *right inset*: calculated reflectance spectrum

In addition, the reflectance also strongly increases with a growing refractive index difference Δn between the layers. In the AlAs/GaAs system on GaAs substrates ($\lambda = 1.55$ µm, $\Delta n = 0.5$, $n_{AlAs} = 2.9$, $\alpha_{AlAs} = 3\,cm^{-1}$, $n_{GaAs} = 3.4$, $\alpha_{GaAs} = 6\,cm^{-1}$) we found a maximum spectral reflectance R_{max} of 0.996 for $p = 20$ and it reached 99.8% for $p \geq 22$. In the AlGaInAs/AlInAs system on InP substrates ($\lambda = 1.55$ µm, $\Delta n = 0.3$, $n_{AlGaInAs} = 3.5$, $\alpha_{AlGaInAs} = 4\,cm^{-1}$, $n_{AlInAs} = 3.2$, $\alpha_{AlInAs} = 3.4\,cm^{-1}$) we found $R_{max} = 0.9993$ for $p = 44$ and it exceeded 99.8% at $p > 37$. Another calculation in the latter material system shows that for different compositions and a low refractive index contrast, the number of periods required is considerably increased: for the AlGaInAs/AlGaInAs system on InP substrates ($\lambda = 1.55$ µm, $\Delta n = 0.18$, $n_{AlGaInAs,I} = 3.42$, $\alpha_{AlGaInAs,I} = 4\,cm^{-1}$, $n_{AlGaInAs,II} = 3.24$, $\alpha_{AlGaInAs,II} = 3.4\,cm^{-1}$) we found $R_{max} = 0.999$ for $p = 70$ and it reached 99.8% for $p > 58$. In the AlGaInAs material system, a higher refractive index contrast can be obtained in contrast to the GaInAsP system without unacceptable loss in the low band-gap layers of the DBRs. Thus, the number p required to exceed the reflectivity of 99.8%, for instance, is larger in GaInAsP than in AlGaInAs. Anyway, in both systems, a relatively large number of periods is required, which is an enormous challenge for the epitaxy. In order to reduce p, the contrast Δn has to be increased considerably. The AlAs/GaAs system seems to be very attractive for DBRs but it involves additional technological difficulties in the fabrication process arising from the large lattice mismatch with InP substrates.

According to Fig. 2, the dielectric Si_3N_4/SiO_2 system ($\lambda = 1.55$ µm, $\Delta n = 0.47$, $n_{Si_3N_4} = 1.94$, $\alpha_{Si_3N_4} = \alpha_{SiO_2}$ both varied, $n_{SiO_2} = 1.47$) provides $R_{max} > 0.998$ already for $p \geq 12$ if loss is neglected. For $\alpha_{Si_3N_4} = \alpha_{SiO_2} = 15\,cm^{-1}$ a reflectivity of 99.8% is exceeded for $p > 14$. In contrast, 99.8% cannot be reached for $\alpha_{Si_3N_4} = \alpha_{SiO_2} = 20\,cm^{-1}$ since R_{max} saturates at $R_{max,sat} = 0.997$. In order to further increase Δn, we studied InP/air-gap structures on InP substrates ($\lambda = 1.55$ µm, $\Delta n = 2.167$, $n_{InP} = 3.167$, $n_{air} = 1$, $\alpha_{InP} = 3.4\,cm^{-1}$), which yield a maximum reflectance of 0.9998 for $p = 4$ and enable R_{max} to exceed 99.8% if $p \geq 3$. Note that three InP/air-gap membranes embedded in air on both sides (in contrast to the previous structure) provide $R_{max} = 0.9996$ for $p = 3.5$ and 0.99993 for $p = 4.5$. This shows that an air 'substrate' instead of an InP substrate provides a much higher R_{max} already for smaller p. Hence, the presence and type of a substrate markedly influence the results, especially for small numbers of periods p.

For the implementation of optical filters, two DBR mirrors have to be combined, the mirrors being separated by a cavity of thickness L. In our case, we mainly study the two material systems shown in Fig. 3. In the case of air cavities, there is no solid medium between the two DBRs (cavity length L). In the case of solid-cavity VCSELs, the central disk on the left is involved, filling the entire cavity. In the case of air-gap cavity VCSELs, the solid disk only partly fills the cavity. This will be explained in more detail in Sect. 7. Nearly all combination possibilities indicated in Fig. 3 have been investigated.

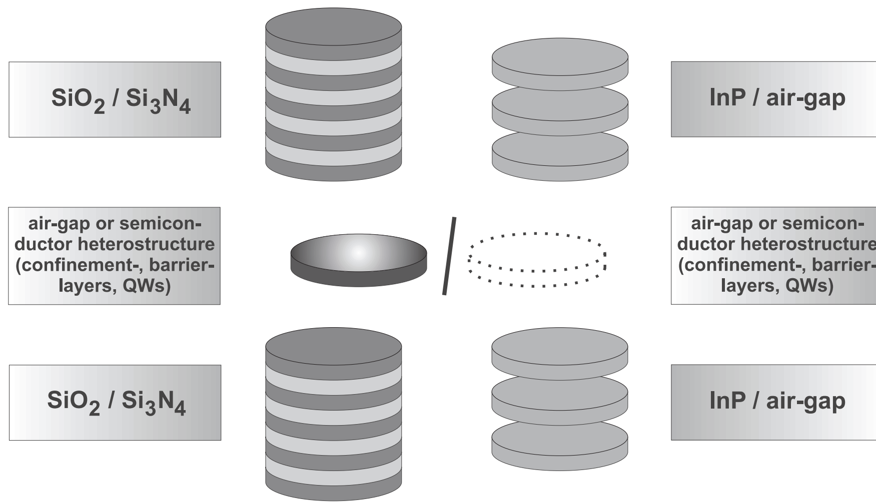

FIGURE 3 Studied filter and VCSEL structures; *left*: all-dielectric DBRs, *right*: semiconductor/ multiple air-gap DBRs

4 Micromachined actuation providing single-parameter tuning

In the case of semiconductor DBRs, electrostatic actuation can be achieved by n-doping of one DBR mirror and by p-doping of the other. Reverse biasing of this p–n junction and varying the voltage enables us to control the cavity length L (Fig. 4). Depending on L, the filter can be adjusted such as to be transparent for only one of the DWDM channels (different vertical arrows) while blocking the others. In Fig. 4a, the top DBR is a circular membrane suspended in the lateral plane by two, three or four suspensions (support beams) of small width. The cross-sectional view (Fig. 4a bottom) intersects from the left to the right: the tilted suspension on the left, the horizontal membrane and the tilted suspension on the right. The tilted suspensions are intended to display the principle in this schematic diagram. In reality, the actuated situation is more complicated, as will be discussed in more detail in Sect. 5.

The optical transmission, calculated as a function of the wavelength for a filter including a 0.5λ air-cavity and two InP/air DBRs ($3\lambda_{InP}/4$ InP, $\lambda_{air}/4$ air, 2.5 periods each), is shown in Fig. 4b. Due to the large refractive index contrast, the stop-band is very large (> 600 nm) and the filter dip has a small spectral line width. Varying the applied voltage enables a spectral tuning of the filter peak (horizontal arrow). As already mentioned in Sect. 2, reductions of the structure size lead both to increasing efficiency of electrostatic actuation and growing stability (Fig. 1). This allows structures to be implemented which look rather brittle if seen with eyes used to our macro world. This holds especially if each DBR is not homogeneously solid, but consists of InP membranes stacked in parallel and separated by air-gaps (multiple air-gap mirror, Fig. 3, right-hand side). The concept for the use of micromachining implies that we obtain a trade-off between maximum tunability and mechanical stability. Suspensions of extremely small width and thickness as well as enormous length would enable very high tuning efficiencies (differential wavelength shift divided by the square of the differential actuation voltage), but guarantee only a minimum mechanical stability. On the other hand, mechanically ultra-stable membranes of enormous thickness and very short suspensions do not yield noticeable tuning efficiencies. Detailed model calculations have shown that InP/air filters with reduced membrane thickness ($\lambda_{InP}/4$ InP, $\lambda_{air}/4$) show higher tuning efficiencies and also extremely large stop-bands of 1500 nm. Unfortunately, these structures have so far been found to be mechanically unstable.

In the case of dielectric DBRs (Fig. 2, left), either additional defined electrodes enable electrostatic actuation or

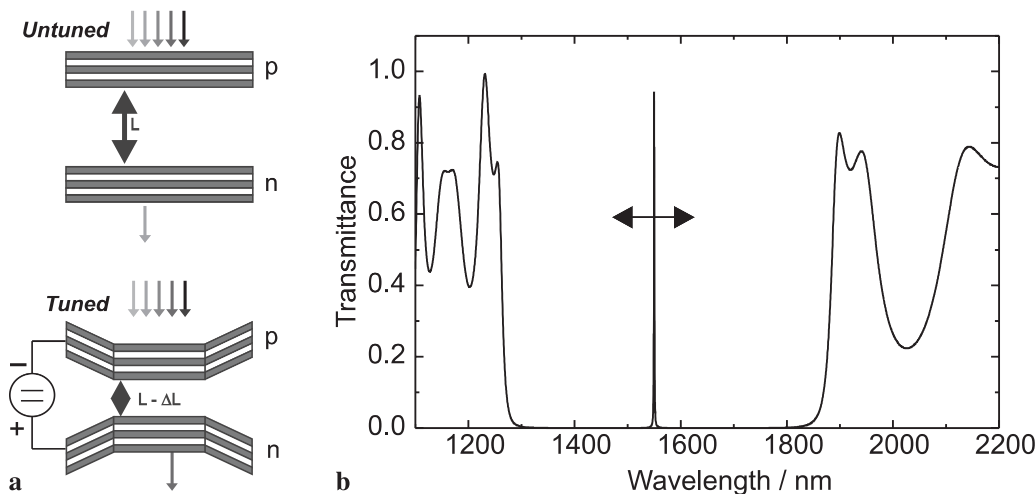

FIGURE 4 **a** Electromechanical tuning principle of optical filters: untuned resonator (*top*), electrostatically actuated cavity (*bottom*), **b** spectral transmission of InP/air-gap filters ($p = 2.5$)

thermal actuation can be brought about by additional defined thin-film heaters [23, 24]. The tuning of our dielectric Bragg mirror devices is achievable by a heating current and, thus, by thermal expansion of the suspensions clamping the dielectric mirror membranes. These air-cavity structures also allow for wide continuous tuning by means of a single control parameter.

5 Technological device fabrication

The implementation of micromachined structures is essentially based on the selective removal of sacrificial layers. Our multiple air-gap filter structures are technologically fabricated using three main steps: (i) definition of the multiple-layer structure by epitaxy or other deposition methods, (ii) dry etching in order to define the lateral structure (vertical patterning of the mesa) and (iii) removing the sacrificial layers by selective wet-chemical underetching to define the air-gaps.

The masks include different membrane geometries as well as strain-indicating structures, quality-control elements and alignment marks. For the four-suspension filter structure (Figs. 5 and 6), the membranes have diameters of 40 μm; the suspensions are 10 μm in width and between 10 μm and 80 μm in length, ending at square supporting posts (150 μm × 150 μm).

5.1 *InP/air-gap filters*

Metal-organic vapor phase epitoxy (MOCVD) is used to grow the multiple-layer structure lattice-matched with (100) *n*-InP substrates: $\lambda_{air}/4$ GaInAs sacrificial layers (defining finally the position of the air-gaps) alternating with $3\lambda_{InP}/4$ InP membranes. The InP layers of the bottom DBR (below the air-gap cavity) are *n*-doped; the InP layers of the top DBR (above the air-gap cavity) are *p*-doped. First, Si_3N_4 is deposited by plasma-enhanced chemical vapor deposition (PECVD) on the epitaxial structure; then a positive resist mask is used in combination with reactive ion etching (5.1 sccm Ar, 3.5 sccm CHF_3, 50 mTorr, 100 W) to define the mask. Figure 5a shows the multiple-layer structure of a single filter element including the black Si_3N_4 mask. 400 filter elements are fabricated at the moment on a wafer area of 10 mm × 10 mm. Outside the black area, the semiconductor surface is uncovered, ready for dry etching. Subsequent reactive ion etching (20 sccm CH_4, 70 sccm H_2, 35 mTorr, 200 W) is used to obtain an etch depth down to ∼ 5.5 μm. Using a Si_3N_4 mask instead of a resist mask guarantees higher selectivity during dry etching and prevents polymer deposition, which is highly undesired on the mesa side walls. This non-selective process provides vertical side walls and sharp, straight edges. Next, the etch mask is removed wet-chemically (HF/H_2O), providing the pure semiconductor mesa (Fig. 5b). For the underetching of the InP membranes the GaInAs sacrificial layers are selectively removed by means of $FeCl_3/H_2O$ so as

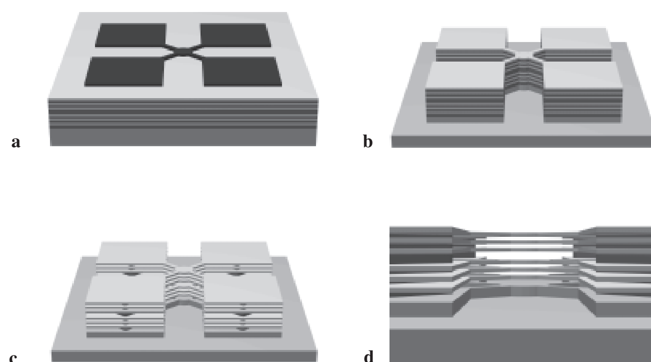

FIGURE 5 Technological implementation of GaInAsP/air-gap filters. **a** mask definition, **b** mesa definition by dry etching, **c** wet-chemical underetching (sacrificial layer removal), **d** side view of underetched filter membranes. The lateral extension of the suspension/membrane region is between 50 and 100 μm. Each supporting post has a lateral size of 150 μm

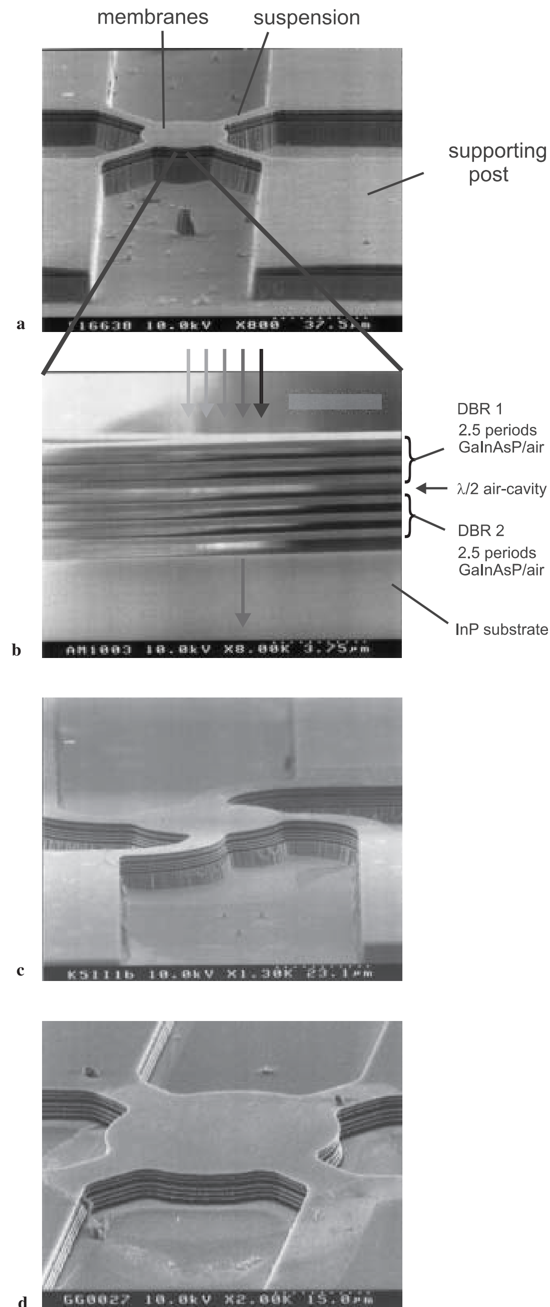

FIGURE 6 Scanning electron micrographs of semiconductor multiple air-gap filters with membranes 30 μm in diameter and four suspensions. **a** 30-μm-long suspensions, **b** blow-up of **a**, **c** spiral-shaped suspensions, **d** 10-μm-long suspensions

to achieve excellent selectivity and good semiconductor/air interfaces (Fig. 5c). At a temperature of $T = 21\,°\mathrm{C}$, an optimized etching time for the above-described structures was found to be 35 min. The membranes and suspensions have to be underetched completely to enable free vertical motion. However, the four support posts are also underetched. This can be avoided by the use of additional masking techniques. Figure 5d depicts a 3D side view of the multiple-membrane filter structure. The three membranes of the top DBR are clearly separated from the three membranes of the bottom DBR. The larger air-gap in the center is the air-cavity.

Figure 6a,c,d display a scanning electron microscope image of a filter structure with four suspensions (resonator details in Fig. 6b). The InP membranes have an optical thickness of $3/4\lambda$. The optical quality of the two surfaces of each membrane is defined by the quality of the epitaxial heterointerfaces. The surface micromachining fabrication process requires no micromounting since the entire structure is fabricated in a batch process. Furthermore, we have a monolithic implementation in the GaInAsP/InP material system. White-light interferometry is used to study the surface morphology with ultra-high spatial resolution (Fig. 7). Note the homogeneous behavior of the four support posts and the four stripe-shaped suspensions among equivalent elements and lateral positions, respectively. The four supporting posts are covered by a protective layer serving to avoid underetching.

In principle, white-light interferometry allows the real bends of the suspensions to be studied. The rather filigree suspensions are found to be continuously bent. However, the main bends are close to the transitions between (i) membrane and suspensions and (ii) suspensions and supporting posts, justifying the schematic depicted in Fig. 4 as a rough approximation. Undesirable bends of the surface membrane can be very well identified. Since the deformation of the bends depends on material parameters, the shape and all geometric parameters of the structure, design involving interferometry is crucial for optimizing the filter function. Special care has to be taken to ensure optimum lattice matching since compressive strain and vertical strain gradients are very critical [25], leading to undesired bends of the underetched membranes.

Since the all-semiconductor devices require high-quality materials and epitaxial processes, the devices have a potential for a very high optical performance. However, the filter can only be a low-cost product if a very large number of devices is batch-fabricated simultaneously. This is guaranteed by the fact that our technological process is compatible with mass production. If, in addition, use is made of cheaper materials, deposition processes and sacrificial layers, the total price may be substantially reduced.

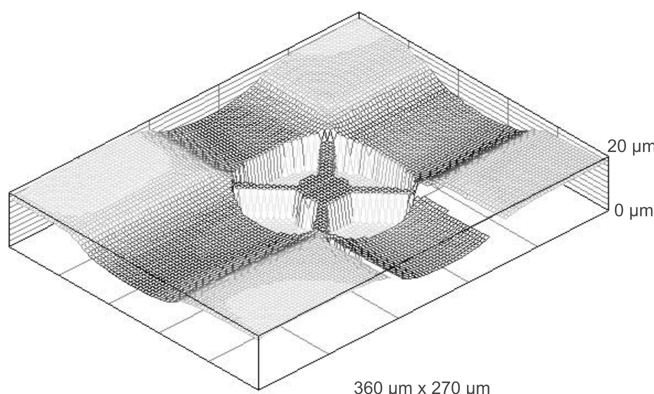

FIGURE 7 White-light interferometric image (Zygo LOT) for a device including 80-μm-long suspensions

The use of Si_3N_4/SiO_2 DBRs in combination with a polymer sacrificial layer enables low-cost filters which also have been fabricated and studied. The dielectric DBRs were deposited by PECVD at low temperatures. The compositions and layer thicknesses of the structure were optimized and controlled, using ellipsometry in combination with transfer matrix model calculations. The sacrificial layers were removed by isopropanol/acetone. Meander-shaped thin-film heaters are defined on the suspensions to allow for thermal actuation of the membranes. In this case, the geometric design of the microstructures is of crucial importance.

6 Results obtained for filter devices

To characterize the filter devices, we use three different set-ups. First, a tunable semiconductor edge-emitting laser with an external resonator (1.46–1.57 μm) and a GaInAs photodiode for monitoring the intensity are employed to characterize the reflectance of the filter devices. This has the advantages of (i) an ultra-high spectral resolution due to the extremely sharp laser line (100 kHz) and (ii) a high signal-to-noise ratio since high spectral power densities can be applied. Second, a white-light source (amplified spontaneous emission of an Er^{3+}-doped fiber amplifier, 1.45 μm to 1.65 μm) is used in combination with an optical spectrum analyzer. Third, as an alternative, a broad-band high-power edge-emitting LED (1.42 μm to 1.7 μm) efficiently coupled to a single-mode fiber and an optical spectrum analyzer is used. The entire set-ups are based on single-mode fibers.

Various filter devices were implemented, having two, three or four suspensions, different membrane diameters and different suspension lengths. In the experiment, a clear correlation was observed between suspension length and tuning efficiency. The shorter the suspensions, the smaller the tunability, as intuitively presumed. By varying the voltage (0–5 V) between the membranes (electrostatic actuation) a tuning range of about 110 nm was obtained for a large number of devices. In the case of two filter devices, tuning ranges of 130 nm and 127 nm were measured for ΔU approximately equal. Thus, a continuous tuning of $> 8\%$ of the absolute wavelength is obtained. This enormous tuning range even exceeds the spectral width of semiconductor laser gain profiles, typically in the range of 110 nm. The extremely wide tuning $\Delta\lambda$, the very small actuation voltage ΔU as well as the large ratio $\Delta\lambda/\Delta U^2$ are record values to the best of our knowledge. The very low absolute voltage values required are very attractive for low-voltage-based low-cost electronics. As already mentioned, the electrostatic actuation is achieved by reverse biasing of the diode formed by the filter. A reverse current $< 1\,\mu\mathrm{A}$ is used, enabling an extremely low total power consumption. Figure 8 displays the experimental results obtained for a filter having three suspensions of 30-μm length which were measured using the fiber amplifier. The transmission dip of the device is located at $\lambda = 1.628\,\mu\mathrm{m}$ for non-actuated

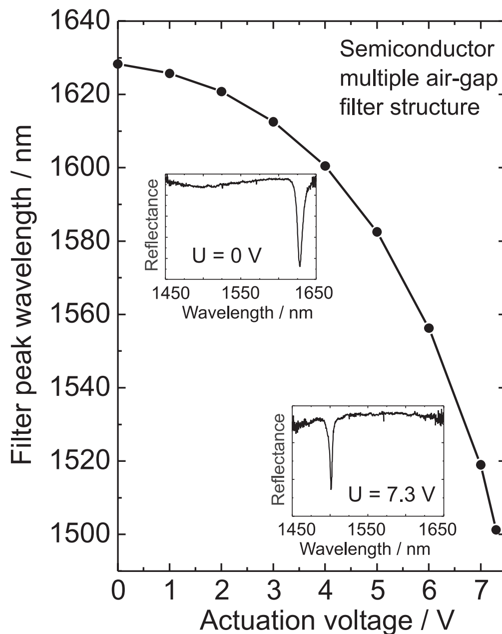

FIGURE 8 Measured electrostatic tuning of a GaInAsP/air-gap filter ($p = 3.5$). *Insets* indicate corresponding spectral reflectance spectra

membranes ($U = 0$ V) and at $\lambda = 1.501$ μm in the case of actuation by $U = 7.3$ V, covering a tuning range of 127 nm. The insets indicate corresponding spectra of low line widths, i.e. of low values for the full width at half maximum (FWHM). Currently, we measured a minimum value of FWHM = 3.5 nm and a change between 3.5 and 4.5 nm across the entire tuning range. For the filter displayed in Fig. 8, the FWHM varies between 3.7 and 7.7 nm. Corresponding model calculations yield a FWHM of 0.8 nm. For the purpose of reducing the line widths, optimizing design and technology are under way. Increasing both the number of periods and the cavity length as well as reducing residual membrane bending would result in a reduction of the line widths. For a similar all-air-gap filter structure, an insertion loss of −3 dB and line widths as small as 0.4 nm have been reported [17]. Tuning ranges between 20 and 70 nm have been reported in the literature for actuation voltages between 14 and 40 V [5–8, 17].

The correlation of the wavelength and the applied voltage is accurately reproducible and does not depend on increasing or decreasing the voltage used to scan the tuning range. Thus, single-parameter tuning without any hysteresis is achieved. Small degradations observed for structures with very long suspensions will most probably be avoided in the future by improvements in design and technology. We believe that the hysteresis-free tuning is due to the zinc-blende lattice of the III/V semiconductors applied. This lattice is strongly related to the Si and diamond lattices of well-known extremely high stability and thus, guarantees the absence of plastic, inelastic mechanic flow.

Care has been taken during the experiments to ensure maximum mechanical stability in order to avoid noise generated by mechanical vibrations. Noise can, however, also be reduced by miniaturization, thus shifting the mechanical resonance frequency into the range between 10 kHz and several MHz. This leads to considerable reductions of the sensitivity of the system to low-frequency vibrations and acoustic waves.

DWDM systems benefit from the extremely large stop-bands provided by the high refractive index differences and short resonators. A single DWDM channel can pass the low line-width filter while blocking the entire range spanned by the second and third telecommunications windows. It is even possible, without difficulty, to extend this range very much if so desired.

Thus, our filters combine several properties that are very attractive for advanced DWDM systems:

- batch-process fabrication using surface micromachining (no need for micromounting of two DBR mirrors, for instance) and compatibility with mass production (low-cost potential),
- extremely wide continuous and kink-free spectral tuning based on a single control parameter,
- very low absolute actuation voltages, allowing the use of low-voltage and, consequently, low-cost electronics,
- low power consumption,
- ultra-wide stop-bands,
- in the case of the semiconductor filters: (i) materials allow the filters to be integrated with lasers and detectors, including active layers of the same material class, (ii) potential for ultra-long-term stability and no hysteresis in tuning,
- from the system point of view, rectangularly shaped spectral filter lines are highly desirable. Intentional design of DBRs with different air-gap widths allows the spectral shape of the filter transmission peak to be tailored. Since all the vertical dimensions of the filter are defined by epitaxy, chirped DBR mirrors can be produced without additional costs,
- potential for very low spectral line width,
- high potential for functionality,
- possible combination with other optoelectronic devices,
- application in optical communications, measurement technologies and sensorics.

The batch process of surface micromachining has potential for low production costs. Semiconductor epitaxy and III/V semiconductor materials, however, are rather expensive. In cases of mass-market products, the specifications may be reduced. Therefore, we additionally worked on micromachined tunable optical filters based on dielectrics and polymers. Figure 9a displays the spectral reflectance of a Si_3N_4/SiO_2 filter ($p = 5.5$ and $p = 5.0$ facing the Si substrate, suspension length: 40 μm). For the implementation of this low-cost filter, use was made of a cheap polymer sacrificial layer which, to the best of our knowledge, has been done for the first time. Assuming $\alpha_{Si_3N_4} = \alpha_{SiO_2} = 15\,cm^{-1}$, we only reach $R_{max} = 0.97$ and $R_{min} = 0.1$ for a five-period DBR according to Fig. 2. Furthermore, noticeable loss also broadens the spectral width and reduces the maximum of the transmission peak. Experimental results of thermal tuning of this filter are shown in Fig. 9b, revealing $\Delta\lambda/\Delta U = -7$ nm/V. A large number of filter devices have been measured, revealing tuning ranges between 10 and 17 nm. As already mentioned with respect to semiconductor filters, an increase is observed for growing lengths of the suspensions.

Transfer matrix model calculations are used to study micromechanically actuated tuning of filters. The semiconductor all-air-gap filter device consists of symmetrically sus-

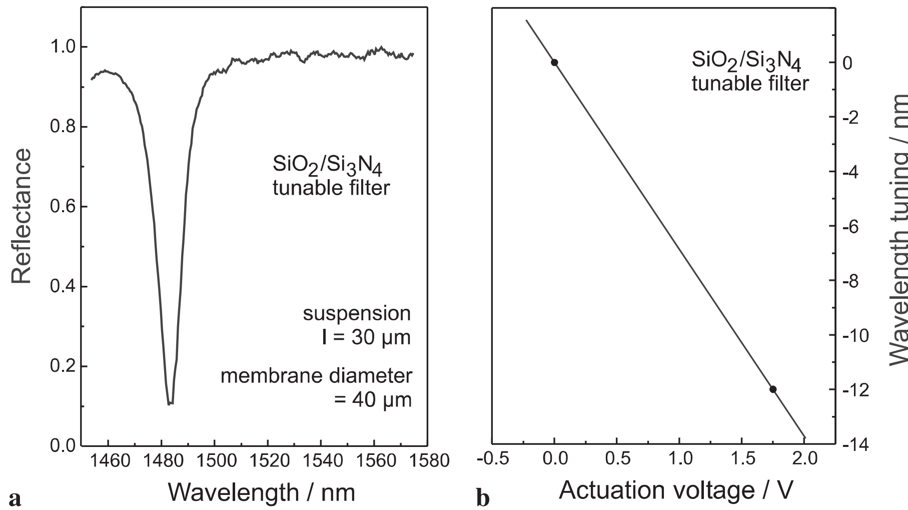

FIGURE 9 Measurements of: **a** spectral reflectance of a Si_3N_4/SiO_2 filter ($p = 5.0$ and 5.5), **b** tuning by thermal actuation as a function of the varied voltage applied to the thin-film heaters

pended InP membranes that are 357 nm in thickness. Neighboring membranes are spaced 375-nm apart from each other in the DBRs. Reflectance spectra are displayed for different air-cavity thickness values L reduced from 830 nm (untuned) to 730 nm in Fig. 10a. Due to the short cavity and the high refractive index difference, the stop-band exceeds 600 nm. For membranes as thin in optical thickness as $\lambda/4$, a stop-band width of even 1500 nm would be possible. This is very attractive for blocking all wavelengths in a very large range of the entire telecommunications band. Figure 10a indicates that all wavelengths in the second and third telecommunications windows can be blocked and a single tunable 'channel' (filter dip) is allowed to pass. We obtain a reflectivity of 99.6% at 1.3 µm, for instance. For a cavity-thickness reduction of $\Delta L = 100$ nm, this calculation provides a spectral tuning of the transmitted wavelength (filter dip) of $\Delta\lambda = 89$ nm, corresponding to a tuning efficiency of $\Delta\lambda/\Delta L = 0.89$.

The structure studied in Fig. 8 is designed for intentional detuning between the center wavelength of the stop-band of the DBR mirrors ($\lambda_{\text{stopband center}}$) and the filter wavelength λ_{filter} (0 V) for non-actuated mirrors. Hoping to achieve a tuning of $\Delta\lambda = 120$ nm, we designed the filter in a way providing λ_{filter} (0 V) $-$ $\lambda_{\text{stopband center}} = 60$ nm. Thus, tuning the filter from λ_{filter} (0 V) to λ_{filter} (7 V) with $\Delta\lambda = \lambda_{\text{filter}}$ (0 V) – λ_{filter} (7 V), we meet $\lambda_{\text{stopband center}}$ rather close to the center of the tuning range. Second, due to the extremely large stop-band widths, this design principle further allows the spectral range close to 1.3 µm (second telecommunications window) to be simultaneously blocked.

Figure 10b depicts the spectral reflectance of an air-cavity Si_3N_4/SiO_2 filter ($p = 11.5$ and 12). Reflectance spectra are displayed for different air-cavity thickness values L reduced from 900 nm (untuned) to 800 nm. The stop-band width is > 300 nm and nearly unaffected by tuning. The transmitted filter peak tunes as much as $\Delta\lambda = 46$ nm due to the cavity-thickness reduction of $\Delta L = 100$ nm, resulting in a tuning efficiency of $\Delta\lambda/\Delta L = 0.46$.

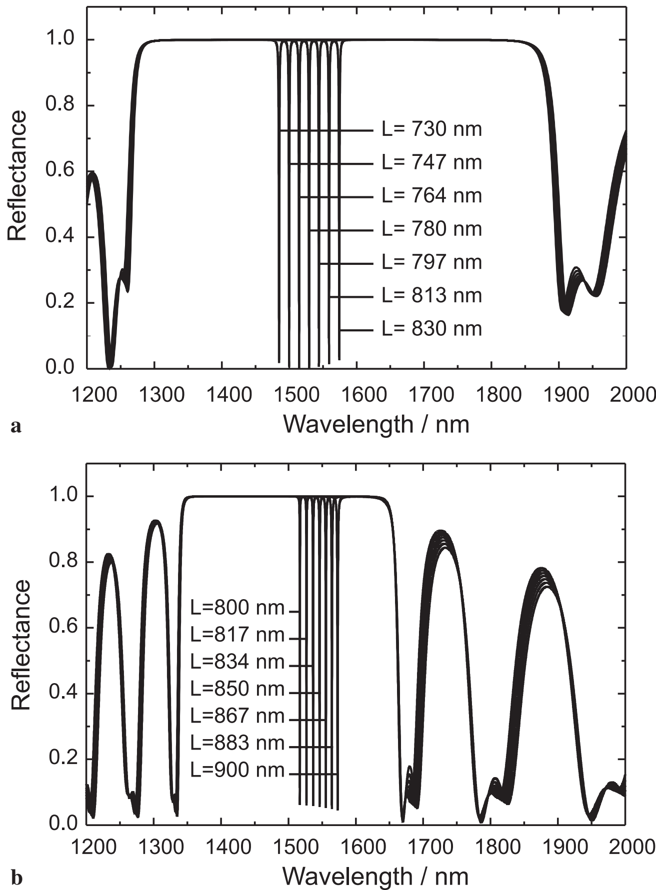

FIGURE 10 Spectral reflectance of tunable air-cavity filters calculated for **a** GaInAsP/air-gap DBRs and **b** Si_3N_4/SiO_2 DBRs. The width of the air-cavity L is varied

7 Results obtained for VCSEL devices

System applications often require a wide continuous spectral tunability of up to 100 nm, sometimes even beyond 100 nm. For edge-emitting lasers, this is very difficult to achieve without macro- or micromechanical actuation. Very effective widely tunable laser devices have been reported in the literature, such as the super-structure grating laser [26–28], the sampled grating laser [29], the Y-laser [30] or codirectionally coupled lasers [31, 32]. However, all these devices require more than a single control parameter (typically three or four different control currents) and very often

they are subject to mode-jumps (discontinuous tuning) or very strong variations of the line width and output power across the tuning range. This complexity often requires a time-consuming detailed characterization of each particular device and subsequent recording of all data. Thus, a microprocessor equipped with individual memory is necessary for each device to control the output wavelength. Micromechanically actuated devices may provide such a wide continuous tuning range under low power consumption and simple control (a single control parameter, most probably no microprocessor).

Air-gap cavity VCSELs including Si_3N_4/SiO_2 DBRs ($p = 11.5$ and 12) and GaInAsP multiple QW active layers were studied. Three active regions, each consisting of two 7-nm-wide GaInAsP QWs, are embedded in four bulk GaInAsP confinement layers. Together with two sandwiching InP cladding layers this stack has either a total thickness of 1.75λ (Fig. 11) or 2λ (Fig. 12). Thus, the entire structure (Figs. 11a and 12a) consists of the following sequence: DBR1 ($p = 12$), the InP/GaInAsP/InP stack (including the QWs), an optional Si_3N_4 antireflection (AR) layer of thickness $\lambda/4$, the air-gap (thickness L') and DBR2 ($p = 11.5$). The cavity length L comprises all layers between the two DBRs. Hence, the cavity has a solid part (including the QWs) and the air-gap part having a vertical extension of L'. Model calculations varying the air-gap thickness L' are performed to study the corresponding tuning properties. Figures 11a and 12a further display the corresponding electric field distribution inside the resonator. For comparing the field amplitudes, the calculated results are related to the total power. The three QW active layers are designed to be located at the antinodes of the electric field. In both structures, we varied the air-gap thickness between 0.44λ and 0.56λ ($\Delta L = 0.12\lambda = 186$ nm, calculated for micromachined actuation) and found a strong shift of the laser peak (corresponding to the dip of small FWHM in the stop-band) in the reflectance spectra (Figs. 11b and 12b). The uncoated VCSEL (Fig. 11) reveals a tuning range of $\Delta\lambda = 101$ nm for a reduction of the air-gap by $\Delta L = 0.12\lambda = 186$ nm. The single-sided AR-coated air-cavity VCSEL (Fig. 12) reveals a tuning range of $\Delta\lambda = 55$ nm for the identical actuation. This results in tuning efficiencies of $\Delta\lambda/\Delta L = 0.54$ and 0.3, respectively. Differences between the structures were also found in the minimum reflectivities $R_{min} \approx 0.4$ (Fig. 11) and $R_{min} \approx 0.1$ (Fig. 12) at the laser wavelengths. Additionally, the uncoated laser enables only a medium lasing efficiency because the maximum electric field at the QW active layer is only 135 a.u. In contrast, the AR-coated VCSEL has a maximum electric field of 270 a.u. Since the number of QWs is identical in both structures, this ensures a better lasing efficiency for the AR-coated VCSEL but a higher tuning efficiency for the uncoated laser. Therefore, a trade-off is observed between either the optimization of the tuning efficiency or the lasing efficiency.

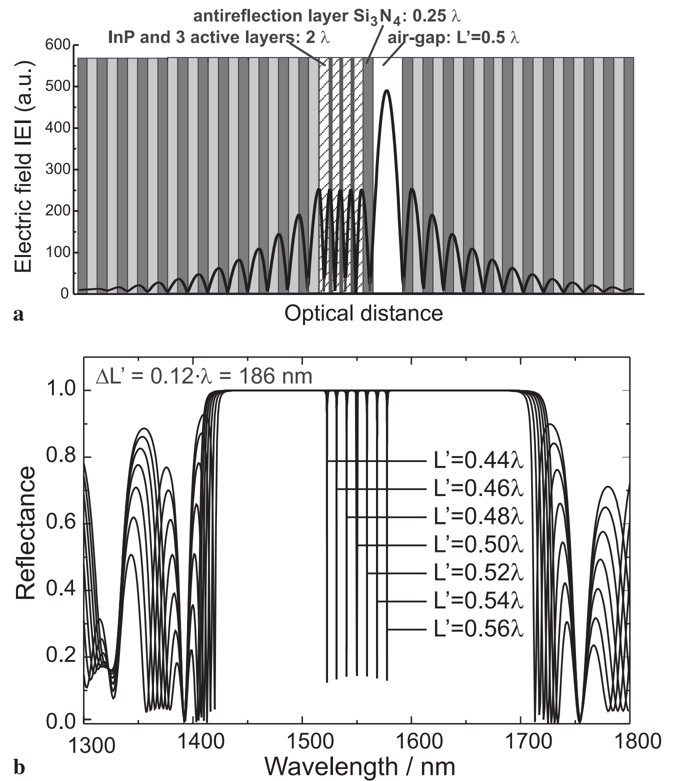

FIGURE 12 Tunable air-cavity GaInAsP VCSEL with Si_3N_4/SiO_2 DBRs and antireflection-coated cavity. **a** Structure and calculated optical field distribution, **b** calculated spectral reflectance for differently tuned air-cavity L'

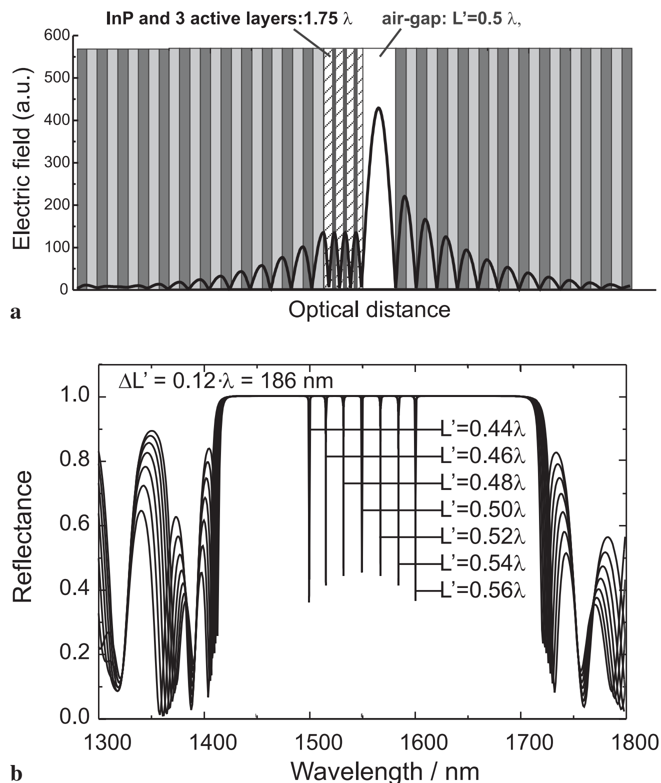

FIGURE 11 Tunable air-cavity GaInAsP VCSEL with Si_3N_4/SiO_2 DBRs and uncoated cavity. **a** Structure and calculated optical field distribution, **b** calculated spectral reflectance for differently tuned air-cavity L'

Finally, optically pumped GaInAsP/Si_3N_4-SiO_2 VCSELs, equivalent to the VCSELs studied above, but without air-cavity, were investigated. Single-mode oscillation at $\lambda = 1.57$ µm, side mode suppression ratio > 40 dB, FWHM < 0.1 nm were measured, using a semiconductor pump laser ($\lambda = 980$ nm, pulsed) for $T = 300$ K. A maximum output

power of $> 75\,\mu W$ was found at 290 K. The lasers were mounted on Au-plated Cu heat sinks, using In-based soldering. The solder-layer thickness was minimized both by mechanical support and wet-chemically, avoiding noticeable oxide layers.

8 Conclusions

Optical, mechanical and electronic components are optimized by tailoring characteristic structure sizes according to key quantities of fundamental physics during the design process. Physics behind recipes for success in nature are imbuing models for scientists and engineers who are using advanced and interdisciplinary methods. Nature provides such an example of tailored scaling: a principle of success in nature is mutation and selection. Proper scaling in natural photonic crystals and our artificial 1D photonic crystals (DBR resonators) determines the wavelength range of diffractive interaction. In addition, proper scaling enhances the mechanical stability and effectiveness of electrostatic and thermal tuning. These basic physical principles are demonstrated in detail by micromachined 1.55-μm vertical-resonator-based devices (optical filters and VCSELs). The devices enable both wide tunability based on a single control parameter and highly reflective DBRs.

(I) Using the InP/air-gap technology, only three membranes per mirror (i.e. three Bragg periods) are sufficient to guarantee reflectivities exceeding 99.8% and to offer enormous stop-band widths > 600 nm. The circular membranes are positioned by two, three or four suspensions, located between air-gaps and stacked in parallel. Micromechanical tuning is obtained by changing the air-gap cavity by means of electrostatic actuation. The structures are technologically fabricated by surface micromachining, using sacrificial layers and avoiding expensive mechanical alignment of the devices by batch processing. Record tunabilities up to 130 nm are reported experimentally for actuation voltages about 7 V. For VCSELs, the air-gap technology offers two main advantages: implementation of Bragg mirrors and active layers within the GaInAsP/InP system and wide continuous tuning.

(II) Based on 12 periods of Si_3N_4/SiO_2 and a polymer sacrificial layer for implementing the air-cavity, we fabricated low-cost optical filters capable of thermally actuated tuning of $\Delta\lambda/\Delta U = -7$ nm/V.

For applications in optical communications and sensorics, the multiple air-gap concept includes the following advantages: batch-process fabrication using surface micromachining, low-cost potential, ultra-wide continuous and kink-free spectral tuning based on a single control parameter, very low absolute actuation voltages, good compatibility with low-cost electronics, extremely low power consumption, ultra-wide stop-bands, potential for a very low spectral line width, high potential in functionality and possible integration with other optoelectronic devices.

ACKNOWLEDGEMENTS Support by the German DFG and BMBF funding under Contract Nos. 01BC150 and Hi763/1-1, respectively, is gratefully acknowledged. Part of the work was performed under the umbrella of the European TUNVIC research project. The authors wish to thank K. Streubel, E. Ataro, D. Gutermuth, H. Schröter-Hohmann, I. Wensch, P. Meissner, H. Halbritter, F. Riemenschneider, N. Chitica, H. Engelhardt, O. Richter, T. Scholz, S.L. Lau, M. El-Hadidy and A. Pun-Utaiwat for technical support, simulation results and stimulating discussions.

REFERENCES

1 M. Born, E. Wolf: *Principles of Optics* (Pergamon, Oxford 1959 and Cambridge University Press 1997)
2 J.E. Lilienfeld: US Patent No. 1 745 175 (1926); US Patent No. 19 000 118 (1928)
3 R. Hilsch, R.W. Pohl: Z. Phys. **111**, 399 (1938)
4 M.C. Larson, J.S. Harris, Jr.: IEEE Photon. Tech. Lett. **7**, 1267 (1995); M.C. Larson, B. Pezeshki, J.S. Harris, Jr.: IEEE Photon. Tech. Lett. **7**, 382 (1995)
5 E.C. Vail, M.S. Wu, G.S. Li, L. Eng, C.J. Chang-Hasnain: Electron. Lett. **31**, 228 (1995); M.S. Wu, E.C. Vail, G.S. Li, W. Yuen, C.J. Chang-Hasnain: Electron. Lett. **31**, 1671 (1995)
6 A. Spisser, R. Ledantec, C. Seassal, J.L. Leclercq, T. Benyattou, D. Rondi, R. Blondeau, G. Guillot, P. Viktorovitch: IEEE Photon. Tech. Lett. **10**, 1259 (1998)
7 P. Tayebati, P. Wang, M. Azimi, L. Maflah, D. Vakhshoori: Electron. Lett. **34**, 1967 (1998)
8 J. Peerlings, A. Dehe, A. Vogt, M. Tilsch, C. Hebeler, F. Langenhan, P. Meissner, H.L. Hartnagel: IEEE Photon. Tech. Lett. **9**, 1235 (1997)
9 D.I. Babic, K. Streubel, R.P. Mirin, N.M. Margalit, J.E. Bowers, E.L. Hu: Electron. Lett. **31**, 653 (1994)
10 N.M. Margalit, J. Piprek, S. Zhang, D.I. Babic, K. Streubel, R.P. Mirin, J.R. Wesselman, J.E. Bowers, E.L. Hu: IEEE J. Sel. Top. Quantum Electron. **3**, 359 (1997)
11 J. Boucart, C. Starck, F. Gaborit, A. Plais, N. Bouché, E. Derouin, J.C. Remy, J. Bonnet-Gamard, L. Goldstein, C. Fortin, D. Carpentier, P. Salet, F. Brillouet, J. Jacquet: IEEE J. Sel. Top. Quantum Electron. **5**, 520 (1999)
12 M. Ortsiefer, R. Shau, G. Böhm, F. Köhler, M.-C. Amann: Appl. Phys. Lett. **76**, 2179 (2000)
13 E. Hall, S. Nakagawa, G. Almuneau, J.K. Kim, L.A. Coldren: Electron. Lett. **36**, 1465 (2000)
14 K. Streubel, S. Rapp, J. André, N. Chitica: Electron. Lett. **32**, 1369 (1996)
15 M.C. Larson, A.R. Massengale, J.S. Harris: Electron. Lett. **32**, 330 (1996)
16 M.Y. Li, W. Yuen, G.S. Li, C.J. Chang-Hasnain: IEEE Photon. Tech. Lett. **10**, 18 (1998)
17 J. Daleiden, N. Chitica, M. Strassner, D. Rondi, E. Goutain, J. Peerlings, J. Pfeiffer, R. Riemenschneider, K. Hjort, R. Dantec, T. Benyattou, A. Spisser, J.L. Leclercq, P. Viktorovitch: In: Proc. Conf. InP Relat. Mater., 1999, pp. 285–287 [ISBN 0-7803-5562-8]
18 D. Vakhshoori, P. Tayebati, C.-C. Lu, M. Azimi, P. Wang, J.-H. Zhou, E. Canoglu: Electron. Lett. **35**, 1 (1999)
19 M. Strassner, J. Daleiden, N. Chitica, D. Keiper, B. Stålnacke, D. Greek, K. Hjort: Sens. Actuators **85**, 249 (2000)
20 N. Chitica, M. Strassner: Appl. Phys. Lett. **78**, 3935 (2001)
21 R. Floyd, C.J. Chang-Hasnain, G.S. Li, R.F. Nabiev, W. Yuen, M. Jansen, D.D. Davis, Jr.: Photonics West 2002, (SPIE Proc. 4649), paper 4649-08, San Jose, USA Jan. 21.–25. 2002
22 B.E. Volland, H. Heerlein, I. Kostic, I.W. Rangelow: Microelectron. Eng. **57**, 641 (2001)
23 H. Hillmer, B. Klepser: Proc. SPIE **3688**, 308 (1998)
24 B. Klepser, H. Hillmer: J. Lightwave Technol. **16**, 1888 (1998)
25 N. Chitica, M. Strassner, J. Daleiden: Appl. Phys. Lett. **77**, 202 (2000)
26 Y. Tohmori, Y. Yoshikuni, H. Ishii, F. Kano, T. Tamamura, Y. Kondo: Electron. Lett. **29**, 352 (1993)
27 H. Ishii, H. Tanobe, F. Kano, Y. Tohmori, Y. Kondo, Y. Yoshikuni: IEEE J. Quantum Electron. **QE-32**, 433 (1996)
28 H. Ishii, F. Kano, Y. Tohmori, Y. Kondo, T. Tamamura, Y. Yoshikuni: IEEE J. Sel. Top. Quantum Electron. **1**, 401 (1995)
29 V. Jayaraman, Z.-M. Chuang, L.A. Coldren: IEEE J. Quantum Electron. **QE-29**, 1824 (1993)
30 M. Schilling, K. Dütting, W. Idler, D. Baums, G. Laube, K. Wünstel, O. Hildebrand: Electron. Lett. **28**, 1998 (1992)
31 P.-J. Rigole, S. Nilsson, L. Bäckbom, T. Klinga, J. Wallin, B. Stålnacke, E. Berglind, B. Stoltz: IEEE Photon. Technol. Lett. **7**, 697 (1995)
32 M. Öberg, S. Nilsson, K. Streubel, J. Wallin, L. Bäckbom, T. Klinga: IEEE Photon. Technol. Lett. **5**, 735 (1993)